



Model for polymerization and self-deactivation in two-photon nanolithography

JASON E. JOHNSON, YIJIE CHEN, AND XIANFAN XU* 

School of Mechanical Engineering and Birck Nanotechnology Center, Purdue University, 1205 W. State St., West Lafayette, IN 47907, USA

*xxu@ecn.purdue.edu

Abstract: A mathematical model is developed to describe the photochemical processes in two-photon nanolithography, including two-step absorption leading to initiation and self-deactivation of the photoinitiator by laser irradiance, polymer chain propagation, termination, inhibition, and inhibitor and photoinitiator diffusion. This model is solved numerically to obtain the concentrations of the reaction species as a function of time and space as a laser beam is scanned through a volume of photoresist, from which a voxel size or linewidth is determined. The most impactful process parameters are determined by fitting the model to experimentally measured linewidths for a range of laser powers and scanning speeds, while also obtaining effective nonlinearities that are similar to previously measured values. The effects and sensitivities of the different process parameters are examined. It is shown that the photopolymerization process is dominated by diffusion of photoinitiators and oxygen inhibitors, and that self-deactivation can lead to higher effective nonlinearities in two-photon nanolithography.

© 2022 Optica Publishing Group under the terms of the [Optica Open Access Publishing Agreement](#)

1. Introduction

Understanding the reaction mechanisms in the photopolymerization process has been an area of research focus for decades, primarily relating to polymerization of films by UV radiation [1–7]. The ability to locally regulate the reaction through control of the light source has also led to photopolymerization's frequent application in 3D additive processes [8–10]. Typically, the photopolymerization reaction is initiated by absorption of a single photon from a UV light source. This linear absorption process inherently limits the resolution to the 2D plane, and additional methods must be applied to regulate the depth of the polymerization [11–13]. Alternatively, increasing the effective nonlinearity of the initiation process can confine the polymerization region, thereby increasing the resolution beyond that obtainable with the linear one-photon absorption processes. Multiple methods have been proposed for increasing the nonlinearity of the printing process [14,15], but the most common of these is multi-photon nanolithography (MPL) [16,17].

In MPL, two or more photons from a high peak-intensity ultrafast laser are simultaneously absorbed by the photoinitiator to initiate the polymerization process. As a result, the exposure dose in the photoresist is proportional to the light intensity to the power of n , where n is the order of absorption. Therefore, for higher orders of absorption, the off-focal components of the intensity dependent dose are suppressed, and any above threshold doses can be limited to a smaller region [18]. This leads to a polymerized volume, or voxel, that can be confined to within the diffraction limited focal spot of the laser excitation source and can be arbitrarily placed within the volume of the photoresist. Typically, in MPL, any means by which the nonlinearity of the process can be increased, further confining the voxel, is treated as analogous to increasing the effective order of absorption. The resolution and design freedom offered by the multi-photon polymerization process has led to fabrication of 3D structures with sub-micrometer resolutions, which have

found applications in areas such as bioengineering [19,20], nano-photonics [21,22], micro-optics [23–25], microfluidics [26,27], micro-electromechanical systems [28], and mechanical metamaterials [29].

As the MPL field continues to advance, there has been a focus on improving the speed of the process. This has led to the introduction of many unique implementations of MPL [30–33]. To further improve the speed, accuracy, and expand applications, it is useful to improve understanding of the underlying kinetics and to have a model for the entire MPL process. While the abundant, comprehensive studies on single photon photopolymerization have been crucial to advances in multi-photon lithography, it has been shown that the reaction kinetics and dynamics in these applications are not entirely analogous to those occurring in MPL. The shorter time scales and smaller reaction volumes of the multi-photon polymerization process lead to different contributions from the reaction's components, primarily oxygen [34]. Furthermore, the complex excited state dynamics that contribute to the effective nonlinearities desired in the MPL process can lead to unanticipated outcomes, such as lower orders of absorption than those suggested by experimental results [35]. Conversely, multi-step absorption processes can be harnessed to further improve the resolution of MPL [36,37] or bypass it entirely [15]. Numerous models have sought to describe the polymerization kinetics in the MPL process [34,38–42]. However, despite the importance often attributed to the effective nonlinearity in experimental studies, these models often assumed the order of the MPL process to be $n = 2$. Any higher order nonlinearities have been implemented by simply raising the writing beam intensity profile, I , to a power, n , greater than two, i.e., I^n with $n > 2$ [38]. Additionally, these models did not consider the complexity of the excited state kinetics which occur during the MPL process. While rate-equation models for excited state kinetics have been implemented for MPL [35] and other two-color lithography (2CL) processes [15], to our knowledge, they have not been integrated with a full photopolymerization model. In this study, a numerical model of 3D nanolithography by two-photon polymerization (TPP) is presented. The model simulates both the excited state kinetics of a multi-step absorption process and the subsequent polymerization kinetics of the photopolymerization process. By simulating the concentration of photoinitiators in the triplet state any intermediate steps within the initiation process that involve this excited state can be studied. The recently presented self-deactivation process [35] is an example of a two-step absorption process which involves the triplet state, and it is the multi-step process considered in this model. In the self-deactivation process, the nonlinearity is increased due to single-photon absorption of the writing laser by the photoinitiator while in the triplet state. A detailed discussion on the implementation of this self-deactivation process is given in Sec. 3. A method for determining the unknown model parameters is presented, where the simulation results are fit to experimentally measured linewidths for a range of laser powers and speeds, while also obtaining effective nonlinearities that are similar to previously measured values. The model is then used to identify the most critical physical processes in the 3D nanolithography process when self-deactivation is occurring.

2. Experimental method

The photoresist used in this study is 2-isopropylthioxanthone (ITX, Sigma-Aldrich) in pentaerythritol triacrylate (PETA, Sigma-Aldrich). The photoinitiator, ITX, was added to the monomer, PETA, with a concentration of 1.5 wt%. The nanolithography was performed with a custom-built system, the details of which have been reported previously [43]. A simplified schematic of the experimental system is shown in Fig. S1(a). A Ti:sapphire femtosecond oscillator (Coherent Micra-10), with an 800 nm center wavelength and an 80 MHz repetition rate, was used as the excitation source. A custom-built prism compressor is used for dispersion pre-compensation. The laser pulse at the print plane was measured by an autocorrelation measurement and was determined to have a FWHM width of ~485 fs. The beam was focused into the photoresist using a 100X oil immersion objective lens (Nikon, $NA = 1.49$). A gold bead scan was performed to

measure the focal intensity distribution [44]. Fitting this distribution with a Gaussian profile, the beam waist of the laser after the objective lens was determined to be ~ 388 nm. The power of the laser was adjusted by the combination of a half-wave plate and a linear polarizer. The laser power was measured just before the back of the objective lens through a 6 mm aperture to replicate the entrance pupil of the objective lens. Powers at the print plane, $P(t)$ shown in Fig. 1(a), were calculated according to the 70% transmission of the objective lens. A piezo-actuated tip/tilt mirror was used to scan the laser beam a length of $80\ \mu\text{m}$ through the photoresist to polymerize single voxel-wide lines. To allow for repeatable positioning of the z -axis, a helium-neon (HeNe) laser was introduced to the 800 nm laser beam path for focus detection at the print plane. The sample photoresist volume was prepared by placing a drop of photoresist in a $\sim 40\ \mu\text{m}$ tall gap between a microscope slide and a coverslip. A schematic of a mounted sample is shown in Fig. S1(b).

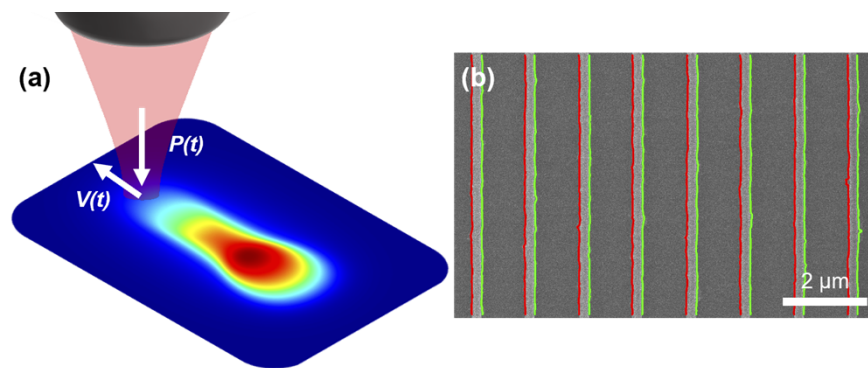


Fig. 1. Two-photon lithography by the scanning of a femtosecond laser through a photoresist. (a) Schematic of experimental and simulated printing process, where the laser moves at a speed V through the photoresist with a laser power P . (b) SEM image of printed lines at a laser power of $P = 4.55$ mW and a speed of $V = 100\ \mu\text{m s}^{-1}$ with highlighted line edges from which average linewidths were computed.

Ten $80\ \mu\text{m}$ long lines were printed on the coverslip surface and the average widths of the lines were measured for each experimental data point. Since suspended lines can exhibit large degrees of non-uniform shrinkage [45], while structures on the glass substrate do not [46], the lines were all printed on the surface of the substrate and line heights were not measured. Each of the ten lines were printed at different z -locations; starting at the surface of the substrate and increasing by a 50 nm step for each line. By measuring linewidths at multiple heights, the effects of the varying degrees of shrinkage due to line height and the varying size of the non-embedded laser intensity profile can be reduced. The maximum linewidth should occur when the center of the voxel is adhered to the substrate, and the maximum linewidth should correspond to the maximum linewidth measurement of the 10 lines. As later seen in the experimental results, the difference between the maximum and minimum average measurement for each data point was small, suggesting an insignificant amount of shrinkage for these lines. After writing, the fabricated lines were developed in an isopropanol bath for 20 minutes, rinsed with isopropanol, and blown with nitrogen for drying. Although development procedures can affect the degree of post-development shrinkage [47,48], the shrinkage was assumed to be uniformly small for each data point since the lines were adhered to the coverslip surface.

The developed samples were sputter-coated with ~ 20 nm of a Au/Pd mixture and imaged with a scanning electron microscope (SEM, Hitachi S-4800). Lines printed at $z = 0$ and $z = 50$ nm, were difficult to image due to low polymerization from significant embedding of the laser focal point in the substrate. As a result, only eight of the 10 lines were measured for each data point.

The SEM images were then processed in MATLAB by means of an edge-finding algorithm to repeatedly obtain average linewidths for each printed line. The details of this edge-finding process are discussed in Supplement S2. The processed SEM image of lines printed at 4.55 mW and a speed of $100 \mu\text{m s}^{-1}$ is shown in Fig. 1(b). The measured edges of the lines are highlighted.

3. Model for two-photon polymerization

The two-photon absorption and polymerization processes and the governing chemical reactions for ITX which are considered in this model are illustrated in Fig. 2. The process begins with initiation, when two photons are simultaneously absorbed and the photoinitiator reaches the excited state, where the molecule can then either relax to the ground state via fluorescence or to the triplet state through intersystem crossing. ITX is a special Norrish Type II photoinitiator that does not always require a coinitiator [36]. Instead, while in the triplet state, ITX can abstract hydrogen from the monomer and create a radical. This radical generation by hydrogen abstraction has two competing processes: phosphorescence and self-deactivation [35]. Self-deactivation is a newly proposed explanation for the higher experimentally measured effective order of nonlinearities for ITX polymerization [34,35]. In self-deactivation, inhibition by combination of triplet state absorption and reverse intersystem crossing (RISC), which is typically used to improve resolution through use of an outside light source [37,43,49], occurs due to the writing laser itself. This is supported by the ITX photoinitiator's non-negligible absorption at 800 nm in the excited state [35], its high intersystem crossing yield of 85% [50], and its long triplet lifetimes relative to its singlet lifetimes [44,51]. The absorption spectrum of ITX in toluene [43] is shown in Fig. S3. In the ground state ITX has negligible absorption at 800 nm. However, other thioxanthone derivatives have shown increases in absorption coefficients on the order of $10^4 \text{ M}^{-1} \text{ cm}^{-1}$ when moving from the ground state to the excited state [52].

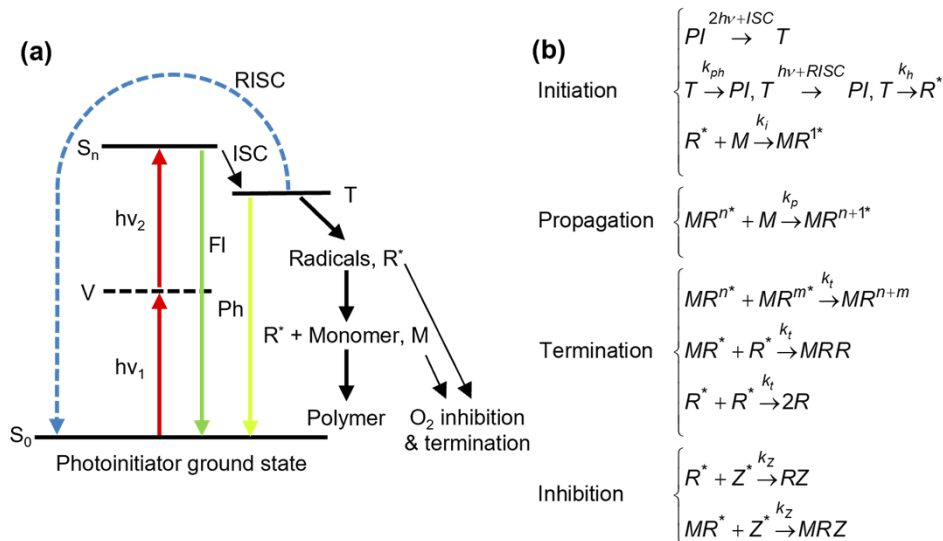


Fig. 2. (a) A simplified Jablonski diagram of two-photon absorption and the subsequent polymerization mechanisms. After two photons are simultaneously absorbed the typical pathways are fluorescence (FI) from the singlet state or intersystem crossing (ISC) to the triplet state, then from the triplet state, phosphorescence (Ph), or radical generation by hydrogen-abstraction. Excited state absorption of the initiating light source can also lead to reverse intersystem crossing (RISC). (b) The reactions involved in the initiation, propagation, termination, and inhibition processes considered in this photopolymerization model.

After a radical is generated, it can react with the free monomers in the resin and create macroradicals, or it can be quenched by oxygen. These macroradicals then react with other free monomers to propagate the polymer chain and create higher crosslinked density polymers or they are quenched by oxygen. The polymerization process is also terminated when two macroradicals react, a macroradical reacts with a radical, or two radicals react with each other. Many of the intermediate steps in the photophysical processes for the ITX photoresist [35] are not considered in the model shown here. Rather, this work presents a simplified model which seeks to understand the effects of the ITX photoreaction on the nanolithography process.

The photopolymerization process described above is mathematically represented by a set of spatiotemporal concentration rate equations. Six reaction species are considered: ground state photoinitiators $[PI]$, triplet state photoinitiators $[T]$, radicals $[R]$, free monomers $[M]$, macroradicals $[MR]$, and inhibitors (oxygen) $[Z]$. Due to the relatively small diffusivities, short lifetimes, or low concentration gradients of some of the species, only diffusions of the photoinitiator and oxygen molecules are considered. A study on the impact of this assumption is included in Supplement S4, and the results are discussed later in this section. The concentrations of ground state photoinitiators and triplet state photoinitiators are described by,

$$\frac{\partial[PI]}{\partial t} = d_{PI}\nabla^2[PI] - \phi_T\sigma_2\Phi^2[PI] + \varepsilon_T\Phi/N_A[T] + k_{ph}[T], \quad (1)$$

$$\frac{\partial[T]}{\partial t} = \phi_T\sigma_2\Phi^2[PI] - \varepsilon_T\Phi/N_A[T] - k_h[T] - k_{ph}[T]. \quad (2)$$

The first term on the right hand side of Eq. (1) is diffusion of the photoinitiator, where d_{PI} is the diffusivity of the photoinitiator. The second term is the generation of triplet state photoinitiators, or triplets, by two photon absorption, where ϕ_T is the triplet quantum yield, σ_2 is the two-photon cross-section, and the photon flux is $\Phi = I(x, y, z, t)/h\nu$. The intensity distribution of the laser is assumed to be perfectly Gaussian. The third term is the self-deactivation term, where ε_T is the excited state molar extinction coefficient in units $M^{-1}cm^{-1}$ and N_A is Avogadro's number. The last term accounts for all pathways from the triplet state back to the ground state. Assuming phosphorescence is the dominant pathway, k_{ph} is the rate coefficient for how this relaxation occurs. In Eq. (2), the triplet state photoinitiator rate equation mirrors the ground state photoinitiator rate equation with one additional term which accounts for the generation of radicals by abstraction of hydrogen according to rate coefficient k_h .

The radical and macroradical concentration rates are, respectively, described by,

$$\frac{\partial[R]}{\partial t} = k_h[T] - k_i[R][M] - k_t[R][MR] - 2k_t[R]^2 - k_Z[R][Z], \quad (3)$$

$$\frac{\partial[MR]}{\partial t} = k_i[R][M] - k_t[R][MR] - 2k_t[MR]^2 - k_Z[MR][Z], \quad (4)$$

where k_i is the kinetic rate coefficient for initiation, k_t is the kinetic rate coefficient for termination, and k_Z is the kinetic rate coefficient for inhibition. The rate for the concentration of oxygen inhibitors is given by,

$$\frac{\partial[Z]}{\partial t} = d_Z\nabla^2[Z] - k_Z[R][Z] - k_Z[MR][Z], \quad (5)$$

where d_Z is the oxygen diffusivity. The rate at which free monomers are used depends on the initiation process with radicals and the propagation process with macroradicals, which occurs according to the kinetic rate coefficient for propagation, k_p , as shown in Eq. (6). Furthermore, if it is assumed all free monomers that react, regardless of the length of the polymer chain they react

with, contribute to the overall degree of monomer conversion, the concentration of converted monomers, C , is the negative of the free monomer concentration as shown in Eq. (7) below.

$$\frac{\partial[M]}{\partial t} = -k_i[R][M] - k_p[M][MR] \quad (6)$$

$$\frac{\partial C}{\partial t} = k_i[R][M] + k_p[M][MR] \quad (7)$$

By numerically solving this system of equations, with an intensity profile that is both pulsing and translating with time, the two-photon nanolithography process for line printing was simulated. The model was solved in MATLAB using a forward time centered space (FTCS) numerical method. The simulated volume's cross-section was set to be sufficiently large to fit the experimentally measured lines (800 nm x 800 nm) and long enough to capture the steady-state line printing process (2 μ m). The photoinitiator and oxygen concentrations were set to a constant value at the boundaries. The degree of conversion was determined by taking the ratio of the converted monomer concentration to the original monomer concentration. The simulated linewidths were obtained by determining the location at which the output spatial profile of monomer conversion is no longer above 20 percent [34,38,53]. To accurately model the experimental results unique to our system, the six most impactful model parameters were varied to fit the experimental results while the remaining were held fixed. Table 1 lists the fixed parameters and their corresponding references. For the kinetic rate coefficient for hydrogen abstraction, only the triplet state lifetime is available in literature, $\tau_T \approx 1 \mu$ s [35,51]. According to Eq. (2), the lifetime of the triplet state after a laser pulse is dependent on the sum of the kinetic rate coefficient for phosphorescence, self-deactivation, and hydrogen abstraction. Thus, the maximum rate of hydrogen abstraction was calculated according to these values and the literature values for the ITX triplet state lifetime.

Table 1. Fixed model parameters

| Parameter name | Symbol | Value | Reference |
|---|------------|--|-------------------------------|
| Free monomer initial concentration | $[M]_i$ | 3900 mol m ⁻³ | Exp. |
| Photoinitiator initial concentration | $[PI]_i$ | 69.6 mol m ⁻³ | Exp. |
| Laser wavelength | | 800 nm | Exp. |
| Repetition rate | | 80 MHz | Exp. |
| Pulse width | | 485 fs | Exp. |
| Beam waist | | 388 nm | Exp. |
| Triplet quantum yield | ϕ_T | 0.85 | [50] |
| Two-photon cross section | σ_2 | 3 GM | [43] |
| Kinetic rate coefficient for hydrogen abstraction | k_h | $1.06 \times 10^5 \text{ s}^{-1}$ | $\tau_T \approx 1 \mu$ s [51] |
| Kinetic rate coefficient for phosphorescence | k_{ph} | $5.9 \times 10^5 \text{ s}^{-1}$ | [51] |
| Kinetic rate coefficient for termination | k_t | $1 \text{ m}^3 \text{ mol}^{-1} \text{ s}^{-1}$ | [54] |
| Kinetic rate coefficient for initiation | k_i | $50 \text{ m}^3 \text{ mol}^{-1} \text{ s}^{-1}$ | [7] |

The six remaining model parameters, listed in Table 2, were determined by minimizing the error between experimental and simulated linewidths, while achieving effective nonlinearities that are similar to previously measured values [34,35]. The Nelder-Mead simplex method was used to minimize the mean squared error between the experimental and simulated linewidths due to its ability to handle nonlinear, non-smooth functions. Within this direct search process, the excited state molar extinction coefficient was first held constant, while the remaining five parameters were varied. The extinction coefficient was then varied to change the effective nonlinearity of the system, due to its high impact on nonlinearity but lower impact on linewidth (discussed in more detail in sections 4.3 and 4.4).

Table 2. Fitting model parameters

| Parameter name | Symbol | Value | Reference |
|--|-----------------|--|---|
| Inhibitor initial concentration | $[Z]_i$ | 4.55 mol m^{-3} | 1 mol m^{-3} [55] |
| Inhibitor diffusivity | d_Z | $2.19 \times 10^{-10} \text{ m}^2 \text{ s}^{-1}$ | $2.27 \times 10^{-10} \text{ m}^2 \text{ s}^{-1}$ [38] |
| Photoinitiator diffusivity | d_{PI} | $2.22 \times 10^{-11} \text{ m}^2 \text{ s}^{-1}$ | $1 \times 10^{-11} \text{ m}^2 \text{ s}^{-1}$ [56] |
| Excited state molar extinction coefficient | ε_T | $60.0 \text{ M}^{-1} \text{ cm}^{-1}$ | $\Delta\varepsilon \in [10^1, 10^4]$ [35,52] |
| Kinetic rate coefficient for propagation | k_p | $2.08 \text{ m}^3 \text{ mol}^{-1} \text{ s}^{-1}$ | $1 \text{ m}^3 \text{ mol}^{-1} \text{ s}^{-1}$ [54] |
| Kinetic rate coefficient for inhibition | k_Z | $3.82 \times 10^4 \text{ m}^3 \text{ mol}^{-1} \text{ s}^{-1}$ | $2300 \text{ m}^3 \text{ mol}^{-1} \text{ s}^{-1}$ [38] |

The effect of including diffusion of the other reactions species was studied in Supplement S4. When it is assumed that triplets and radicals have a diffusivity equal to the photoinitiator diffusivity in Table 2, inclusion of their diffusion terms have a negligible effect on the model. Since the monomer, PETA, has a similar molecular weight to ITX, monomer diffusion was also tested using a diffusivity equal to the photoinitiator. It was found that including free monomer diffusion had a small effect on simulation results except for at higher scanning speeds where higher linewidths were given. Macroradical diffusion was not tested since it is often not considered due to their large molecular weight during propagation [5,57–59].

The oxygen and photoinitiator diffusivities and the kinetic rate coefficients for photopolymerization are assumed to be constant. These rates will vary with degree of conversion and temperature [2]. The small temperature changes within the typical MPL writing regime applicable to this model make the kinetic rate coefficients' temperature dependencies negligible [60]. A detailed study on the effect of this constant diffusivity and kinetic rate coefficient assumption is presented in Supplement S5. Similar to previous studies [38], conversion dependent kinetic rate coefficients decreased degree of conversion uniformly for all writing conditions. A decrease in total degree of conversion of ~3% for all writing conditions led to a 2% and 18.2% shift in threshold power and speed, respectively. Conversion dependent diffusion coefficients led to a 6.8% decrease in threshold power and a 24.2% increase in threshold speed. Although these values are not negligible, they are smaller than other values seen in the sensitivity analysis in Section 4.3, and the primary departures in linewidth results occurred at high speeds where experimental data is limited. In order to simplify the fitting process conversion dependent coefficients were not included; due to the large number of unknown parameters the conversion dependence relationships add to the model. The impact of radical trapping [58] was studied in Supplement S6. A conversion dependent radical trapping term was added to the macroradical concentration rate equation and was found to have negligible effect on linewidth results.

ITX/PETA photoresists have been reported to have effective nonlinearity values ranging between 3 and 4 at 800 nm [34,35]. Numerous techniques have been presented to experimentally determine this nonlinearity [38,61,62], but more recently the 2-beam initiation threshold (2-BIT) technique has been shown to be less susceptible to other nonlinear processes in MPL [63,64]. In the 2-BIT method, two beams which are spatially overlapped and temporally interleaved are used to achieve multi-photon polymerization. By varying the power of each of the beams independently, the threshold powers of the 2-beam system can be determined according to the following relationship,

$$\bar{P}_1^{n_{eff}} + \bar{P}_2^{n_{eff}} = 1, \quad (8)$$

where \bar{P}_1 and \bar{P}_2 are the powers of each of the beams normalized to their threshold values when the other beam is off and n_{eff} is the effective nonlinearity of the system. The model in this study can be used to simulate this experimental process by adding polymerization from a second laser beam. By simulating line writing with two overlapped beams with powers \bar{P}_1 and \bar{P}_2 where the pulses of each beam alternate to create a combined repetition rate of 160 MHz, the threshold

power value for \bar{P}_2 when \bar{P}_1 is fixed, and vice versa, can be determined. Then, from these \bar{P}_1 and \bar{P}_2 values the theoretical effective nonlinearity of the system can be determined for any given set of parameters by fitting Eq. (8) to the results. Using this simulation of the 2-BIT method in combination with the Nelder-Mead method, the values of the six parameters described above were obtained and are listed in Table 2. These parameters describe a system with an effective nonlinearity of $n_{eff} = 2.87$. The literature values in Table 2 for these six parameters were used as reference points during the fitting process.

4. Results and discussion

4.1. Experimental results

Figure 3 shows the experimental results and the computed results obtained using the best-fit parameters listed in Table 2. Figure 3(a) shows the experimental results of the linewidths at different laser powers and a constant laser scanning speed of $100 \mu\text{m s}^{-1}$, while the results in Fig. 3(b) are the linewidths at different scanning speeds and a constant laser power of 4.55 mW at the print plane. Each data point is the mean of the average linewidths for each of the 8 lines printed using those parameters. The error bars correspond to the minimum and maximum average linewidths measured for that data point. For both sets of experimental data in Fig. 3(a) and 3(b), the lines printed near the threshold were not measurable after development. An example of lines with low crosslinking density printed 0.05 mW above the power gelation threshold is shown in Fig. S9. The gelation threshold, or power and scan speed after which no polymerization occurs, was observable and was measured for each case and is marked by the red dashed line in Fig. 3. The trend shown by the experimental data for linewidth versus laser power, in Fig. 3(a), is well captured by the simulation. Similarly, the experimental linewidths for variable laser scanning speeds in Fig. 3(b) match those obtained by the simulation. As the simulation approaches the slower speeds the model begins to diverge from experimental results. This discrepancy is possibly due to the constant diffusion coefficients used in the model. The variable diffusion coefficient results in Fig. S7(b) show a decrease in linewidths at slower speeds. At these slower speeds, where monomer conversion is larger due to the longer periods of exposure (also see Fig. 4(a)), the variation in diffusion coefficients will be greater which could lead to nonlocal effects on oxygen and photoinitiator concentrations ultimately leading to lower linewidths.

Figure 3(c) shows the results in Fig. 3(a) and 3(b) plotted as a function of TPP exposure dose. The exposure dose, D , for photopolymerization is typically defined by the relationship $D \propto \Delta t \times I^n$, where Δt is the exposure time, I is the illumination intensity, and n is the order of absorption. For the scanning line writing configuration and two-photon absorption this relationship can be written as $D \propto \tau f_{rep} P^2 / V$, where τ is the laser pulse width and f_{rep} is the laser repetition rate. This relationship is used to calculate the dose values which are plotted with the linewidths in Fig. 3(c) for the experimental and simulated data points at constant speed and varied power, and at constant power and varied speed. Examining the trends in Fig. 3(c) suggests that a simple logarithmic dependence of linewidth on laser dosage squared, or $d_{line} \propto \sqrt{\ln(D)}$, suggested in many empirical models [65–67], is not sufficient to approximate linewidths. That is, the same dose produces different values of linewidths when different combinations of power and speed are used. The inability of this exposure dose relationship to fully capture the MPL process has been discussed before [38,61]. Instead, the presence of nonlinear processes such as depletion and replenishment of oxygen and photoinitiators lead to a more complex dependence on laser power and scan speed.

4.2. Temporal evolution of reaction species

The results of the simulation can provide insight into the temporal evolution of the species of interest, whereas experimental measurements of their temporal development are challenging. The change in percent monomer conversion and the change in the concentrations of the other five

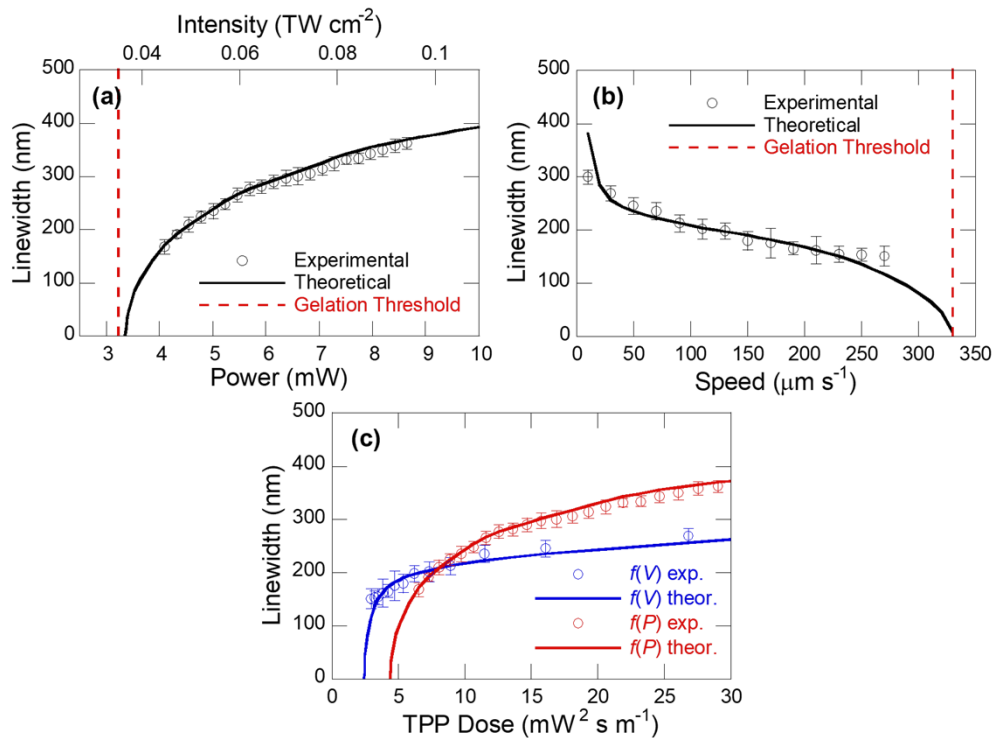


Fig. 3. (a) The experimental data of linewidth versus laser power and the peak laser intensity compared with the results of the numerical simulation. (b) The experimental data of the linewidth versus laser scanning speed compared with the results of the numerical simulation. The experimentally measured gelation threshold is also shown in (a) and (b). Both the laser power and speed theoretical linewidths are determined by finding the location at which the degree of conversion matches the predefined conversion threshold of 20 percent. (c) The experimental and theoretical results for variable speed, $f(V)$, and variable laser power, $f(P)$ plotted as a function of two-photon polymerization dose. The values for dose are determined using the relationship $D = \tau f_{rep} P^2/V$. The error bars correspond to the minimum and maximum linewidths measured for that data point.

reaction components as a function of time are presented in Fig. 4. The printing of a 2 μm long line for five different sets of powers and speeds was simulated. The results at the center of the line's cross-section at 0.5 μm from the starting location of the laser are shown in each figure. The legend is arranged such that the parameter sets are in order of increasing dose.

The monomer conversion over time for each parameter set can be seen in Fig. 4(a). Like linewidths, the total conversion does not scale directly with dose. Instead, the monomer conversion trends are strongly dependent on the oxygen concentration. Figure 4(b) shows the change in oxygen concentrations with time. The oxygen supply is fully depleted in each of the cases, with both the laser power and scanning speed affecting how quickly this depletion and replenishment occurs. The vertical dashed lines in Fig. 4(b) mark the time at which the intensity is greatest for each of the 250, 100, and 50 μm s⁻¹ scanning speeds. For each case, the time at which the monomer conversion in Fig. 4(a) starts and stops increasing corresponds to when the oxygen concentration reaches zero and rises from zero, respectively. The horizontal line in Fig. 4(b) marks 1% of the initial oxygen concentration. The circular markers in Fig. 4(a) represent the conversion at the times when the oxygen concentration is equal to 1% of the initial oxygen concentration.

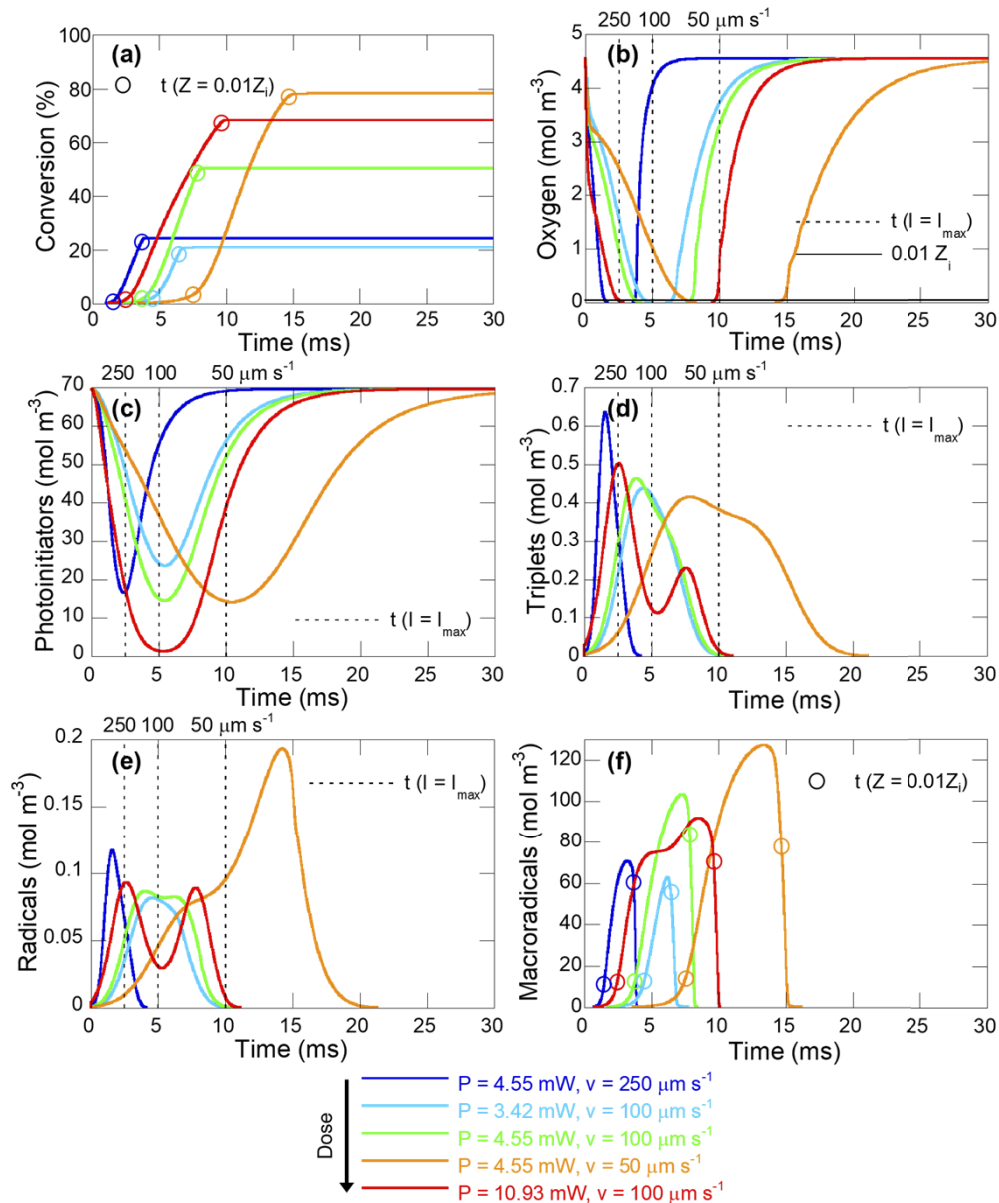


Fig. 4. Simulated temporal development of reaction species for several different process parameters. Five combinations of three different speeds and three different laser powers are used to simulate the printing of a $2 \mu\text{m}$ long line. The change with time at the center of the line's cross-section at $0.5 \mu\text{m}$ from the starting location of the laser in (a) monomer conversion, (b) oxygen concentration, (c) photoinitiator concentration, (d) triplet state photoinitiator concentration, (e) radical concentration, (f) and macroradical concentration are shown. The circle data points included in (a) and (f) are the locations for that set of conditions where the oxygen concentration is at 1% of the initial oxygen concentration. The horizontal line in (b) marks 1% of the initial oxygen concentration. The vertical dashed lines in (b), (c), (d), and (e) represent the times at which the laser intensity is greatest for the 250 $\mu\text{m s}^{-1}$, 100 $\mu\text{m s}^{-1}$, and 50 $\mu\text{m s}^{-1}$ conditions.

When oxygen is depleted and polymerization can continue unquenched, the photoinitiator is the regulating species. The characteristics of the other reaction species' profiles can be correlated to the photoinitiator profile when oxygen is depleted. The varying degree of photoinitiator consumption can be seen in Fig. 4(c). The minimum concentration of photoinitiator throughout the process is strongly correlated with the laser power, with each of the three 4.55 mW cases reaching approximately the same minimum value and the 10.93 mW case almost fully depleting the photoinitiators. For each case the minimum photoinitiator concentration occurs near when the intensity is greatest while the laser beam is directly over the location of interest. This is marked by a dashed line for each speed. If photoinitiator diffusion was not present, the 4.55 mW, 50 $\mu\text{m s}^{-1}$ case, with twice the exposure dose, would reach a lower photoinitiator concentration than the 4.55 mW, 100 $\mu\text{m s}^{-1}$ case. Instead, the diffusivity of photoinitiators from Table 2 results in a characteristic time constant of ~ 1 ms for diffusion from the boundary of the simulation volume. This means the photoinitiator supply is continually replenished and its concentration is only limited by the laser intensity.

The change in triplet concentration, shown in Fig. 4(d), is dependent on triplet generation by two-photon absorption and triplet deactivation by single-photon absorption, as seen in Eq. (2). For each case the rate of generation dominates, with a value no less than approximately twice the rate of deactivation. Upon first incidence of the laser, triplets are generated, then as the photoinitiator supply is reduced the generation of triplets decreases. For all but the 10.93 mW, 100 $\mu\text{m s}^{-1}$ case, the maximum triplet concentration occurs when two photon absorption, the first term of Eq. (2), is at its maximum, shortly before the laser passes over the location of interest (marked by the dashed lines for each print speed). For the 10.93 mW case, this maximum would also occur shortly before the laser passes, at around 4.5 ms, if more photoinitiators were available, however, depletion of the photoinitiator supply instead leads to a local minimum when the minimum photoinitiator supply is reached. Then, as the photoinitiator concentration recovers while the intensity is still nonzero, more triplets are generated, leading to a second peak in the triplet concentration.

Figure 4(e) shows the radical concentration profiles. Radicals are generated by hydrogen abstraction of triplets. As a result, the radical concentration trends are similar to the triplet concentration trends but lessened due to oxygen inhibition. For example, unlike the triplet concentration, the second peak of radical concentration for the 10.93 mW case has a similar magnitude to the first, because the oxygen concentration was not fully depleted until the time when the first peak occurred. Similarly, for the 4.55 mW, 50 $\mu\text{m s}^{-1}$ case, the radicals accumulate to a much greater value due to the longer period during which oxygen is depleted. Figure 4(f) shows the macroradical concentration. Since the macroradical concentration is an accumulation of radicals, the macroradical concentrations follow a dampened radical concentration trend. The circular markers in Fig. 4(f) mark the concentration when oxygen is at 1% of the initial concentration. The macroradicals only accumulate and propagate when oxygen is depleted. Overall, these results suggest oxygen diffusion and replenishment is the dominant process, while photoinitiator related processes dominate only when oxygen is depleted. The dominance of oxygen and photoinitiator concentrations shown here is in agreement with previous experimental studies on MPL polymerization kinetics [34].

4.3. Sensitivity analysis

A sensitivity analysis was performed on the model to determine the impact of each of the fitting parameters and their corresponding processes (Fig. 5). In the sensitivity analysis, a single parameter was varied by $\pm 30\%$ and the linewidths and effective nonlinearity of the system were recalculated. The effect of each parameter on the model is summarized by determining the change in threshold power, ΔP_{th} , threshold scanning speed, ΔV_{th} , and effective nonlinearity, n_{eff} . Figure 5(a) summarizes the resulting changes in threshold values for a $\pm 30\%$ variation in each of

the parameters. Figures 5(b) and 5(c) show the individual changes in threshold speed and power, respectively. From these figures, it is seen that the system exhibits similarly large sensitivity to initial oxygen concentration, $[Z]_i$, and oxygen diffusivity, d_z . Specifically, the system is more sensitive to increases in these parameters, while decreases are slightly less impactful. This is likely because increasing these parameters leads to earlier replenishment of the oxygen supply and as a result more rapid quenching of the entire polymerization process. This is further supported by the larger changes seen for threshold velocities. Alternatively, decreasing oxygen inhibition delays this quenching, but the process is still controlled by photoinitiator supply. Varying the photoinitiator diffusivity, d_{PI} , is impactful on threshold power. Decreasing the photoinitiator diffusivity delays the photoinitiator replenishment process, increases photoinitiator depletion, and leads to lower conversion values before oxygen quenches the process. The two kinetic rate coefficient fitting parameters, k_p and k_z , have smaller impacts on the model, except for the kinetic propagation rate coefficient's (k_p) impact on the velocity thresholds. The kinetic propagation rate coefficient has a direct effect on the rate that monomers react with macroradicals. At higher speeds, it is important that the macroradicals that are quickly generated and quenched react with monomers at a higher rate during their shorter lifetimes. The effect of the deactivation process, i.e., the excited state molar extinction coefficient, ε_T , is similar for threshold speeds and powers. An increase or decrease of the extinction coefficient simply leads to a larger or smaller number of radicals generated by each laser pulse, respectively.

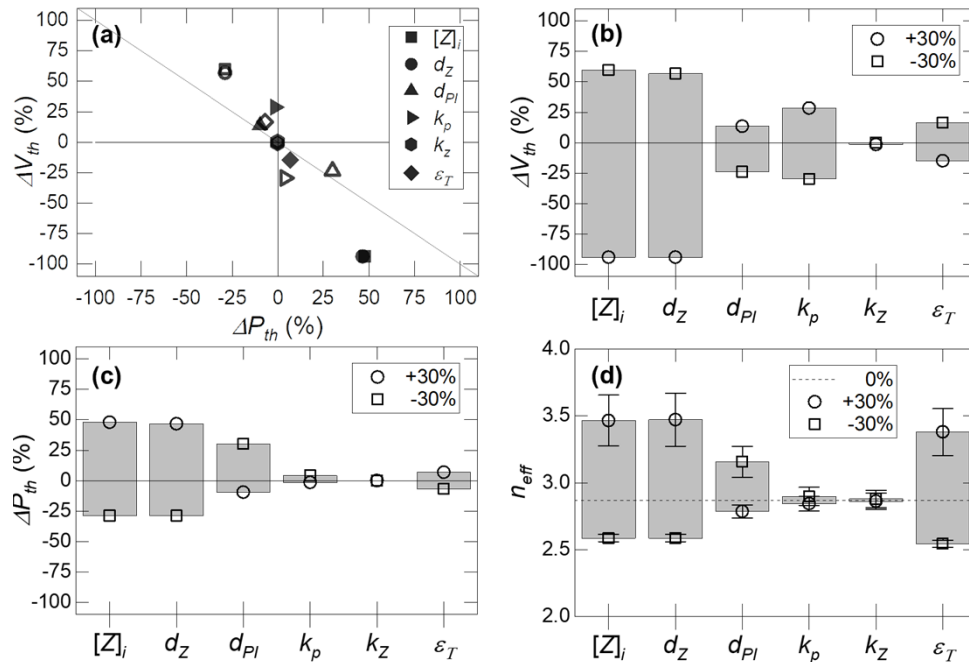


Fig. 5. Sensitivity analysis for fitting parameters. (a) Change in threshold speed and change in threshold power. Filled markers correspond to +30% values and markers without fill correspond to -30% values. A solid gray line is plotted to show where a data point will fall if a variation of that parameter decreases the threshold speed and increases the threshold power an equal percentage. (b) Percent change in threshold speed after varying each fitting parameter $\pm 30\%$. (c) Percent change in threshold power after varying each fitting parameter $\pm 30\%$. (d) Change in effective nonlinearity for a $\pm 30\%$ variation of each fitting parameter. The error bars correspond to the 75% confidence interval for the best-fit n_{eff} value. A dashed line marks the baseline n_{eff} of 2.87.

The changes in effective nonlinearities due to the variation of each parameter are shown in Fig. 5(d). The error bars in Fig. 5(d) correspond to the 75% confidence interval of the best-fit n_{eff} value. From the simulations with higher nonlinearity values, around $n_{eff} > 3$, the 2-BIT relationship given by Eq. (8) begins to break down when self-deactivation is present in the system. The 2-BIT simulation results used to obtain the values in Fig. 5(d) suggest when one of the two beams is low relative to its threshold power, self-deactivation causes it to contribute more to inhibition than initiation, and the threshold power of the other beam is increased due to its presence, or $\bar{P}_1^{n_{eff}} + \bar{P}_2^{n_{eff}} > 1$ for $P_1 \ll P_{1,th}$. This should only occur when multiple orders of absorption contribute to the writing process, as is the case when self-deactivation is present. While non-integer values given by Eq. (8) typically serve as a good approximation for multiple order systems, to model a multiple order system more accurately, a relationship more complex than Eq. (8) is necessary [68]. This leads to the larger confidence intervals seen for the higher nonlinearity values in Fig. 5(d). Figure 5(d) suggests the nonlinearity of the system is very sensitive to changes in the oxygen related parameters and the triplet state absorption controlled by the molar extinction coefficient, ε_T . However, only the excited state extinction coefficient causes a nonlinearity much greater than two. When self-deactivation is not present with an excited state extinction coefficient of $\varepsilon_T = 0$, the nonlinearity is $n_{eff} = 2$ using the other values presented in Table 2, and only increases to 2.004 and 2.003 by increasing the oxygen initial concentration and diffusivity by 30%, respectively.

4.4. Self-deactivation and effective nonlinearity

The effects of the self-deactivation phenomenon were further analyzed by observing how the model changed for various values of excited state molar extinction coefficients. Figure 6 shows the effect of the self-deactivation process on the linewidth versus power trend (Fig. 6(a)) and on the effective nonlinearity of the system (Fig. 6(b)). The mechanism by which self-deactivation occurs, triplet state absorption induced RISC, is the same mechanism through which other works suggest inhibition occurs for 2CL with ITX [37,43,49]. Similar to using an additional inhibition laser to increase the threshold power, the results in Fig. 6(a) show increasing the triplet state absorption of the writing laser somewhat uniformly shifts the linewidth trend and as a result increases the threshold power. It is worth pointing out that, while simulation of the triplet state is applicable to many common photoinitiators in MPL, like DETC [69], the self-deactivation term in Eqs. (1) and (2) can be directly applied to two-color inhibition processes, by changing the molar extinction coefficient and photon flux to values relating to a separate inhibition laser.

Self-deactivation was originally proposed as an alternative explanation to higher order absorption as the cause of high experimentally measured effective nonlinearities of ITX photoresists, and a kinetic model of the electronic state populations of ITX during irradiation has been presented to analyze this theory [35]. Figure 6(b) shows the effective nonlinearities given by the 2-BIT simulation for various extinction coefficients in this study's polymerization model. The trend in Fig. 6(b), for extinction coefficient values from zero to $100 \text{ M}^{-1}\text{cm}^{-1}$, is similar to the results of the kinetic model presented in [35]. As expected, the nonlinearity of the system approaches a value of $n_{eff} = 2$ as ε_T goes to zero. As the extinction coefficient increases past $100 \text{ M}^{-1}\text{cm}^{-1}$, the inhibition effect of the second beam again causes the relationship given by Eq. (8) to break down and the trend is flattened. Nonetheless, simulation suggests that with reasonably low excited state molar extinction coefficient values at 800 nm, self-deactivation can occur and can lead to effective nonlinearities in ranges like those experimentally determined for ITX.

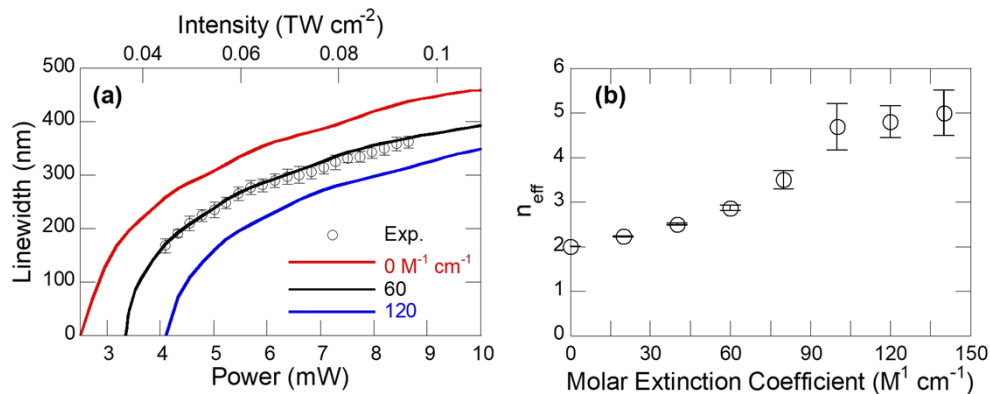


Fig. 6. (a) The simulated linewidth versus power for different molar extinction coefficients. The error bars correspond to minimum and maximum measured linewidths. (b) The effect of the extinction coefficient on the effective nonlinearity of the system. The error bars correspond to the 75% confidence intervals for best-fit n_{eff} .

5. Conclusion

The photopolymerization reaction in two-photon lithography is analyzed via the development of a combined excited state and polymerization kinetics model. The excited state dynamics of the ITX photoinitiator are captured by the model and the inclusion of triplet state absorption simulates the self-deactivation process. The mathematical model developed here can be readily applied to other two-color inhibition processes for sub-diffraction lithography. The different parameters of the simulation are determined by fitting the model to experimentally obtained linewidths and effective nonlinearities. The output spatial polymerization profiles of the model capture the experimentally obtained linewidth trends for both variable powers and variable speeds. The temporal profiles of the reaction components help to explain their development and how depletion and replenishment by diffusion of the photoinitiators and oxygen inhibitors affects the triplet, radical, and macroradical concentrations. A sensitivity analysis of the model also suggests the MPL process is dominated by oxygen and photoinitiator diffusion. The self-deactivation process is shown to produce a shift in the threshold power like that of typical inhibition processes and that reasonable values of excited state molar extinction coefficients at 800 nm can lead to the higher effective nonlinearities previously observed for ITX photoresists. By better understanding the effects of these different model parameters and their respective processes, the polymerization and excited state kinetics of 3D nanolithography by TPP are further elucidated.

Funding. National Science Foundation (CMMI-1634832, CMMI-2135585, DGE-1842166).

Acknowledgments. We would like to thank the support by the U.S. National Science Foundation (CMMI-1634832, CMMI-2135585). Jason E. Johnson acknowledges the U.S. National Science Foundation for support under the Graduate Research Fellowship Program (GRFP) under grant number DGE-1842166. We acknowledge Paul Somers and Mauricio Segovia for helpful discussion and Teng Chi and Prof. B.W. Boudouris for the ITX absorption spectra.

Disclosures. The authors declare no conflicts of interest.

Data availability. Data underlying the results presented in this paper are not publicly available at this time but may be obtained from the authors upon reasonable request.

Supplemental document. See [Supplement 1](#) for supporting content.

References

1. J. P. Fouassier, X. Allonas, and D. Burget, "Photopolymerization reactions under visible lights: Principle, mechanisms and examples of applications," *Prog. Org. Coat.* **47**(1), 16–36 (2003).

2. E. Andrzejewska, "Photopolymerization kinetics of multifunctional monomers," *Prog. Polym. Sci.* **26**(4), 605–665 (2001).
3. C. Decker, "Photoinitiated crosslinking polymerisation," *Prog. Polym. Sci.* **21**(4), 593–650 (1996).
4. S. C. Ligon, B. Husár, H. Wutzel, R. Holman, and R. Liska, "Strategies to reduce oxygen inhibition in photoinduced polymerization," *Chem. Rev.* **114**(1), 557–589 (2014).
5. M. R. Gleeson and J. T. Sheridan, "Nonlocal photopolymerization kinetics including multiple termination mechanisms and dark reactions Part I Modeling," *J. Opt. Soc. Am. B* **26**(9), 1736–1745 (2009).
6. M. R. Gleeson, S. Liu, R. R. McLeod, and J. T. Sheridan, "Nonlocal photopolymerization kinetics including multiple termination mechanisms and dark reactions Part II Experimental validation," *J. Opt. Soc. Am. B* **26**(9), 1746–1754 (2009).
7. M. R. Gleeson, S. Liu, J. Guo, and J. T. Sheridan, "Non-local photo-polymerization kinetics including multiple termination mechanisms and dark reactions: Part III Primary radical generation and inhibition," *J. Opt. Soc. Am. B* **27**(9), 1804–1812 (2010).
8. S. C. Ligon, R. Liska, J. Stampfl, M. Gurr, and R. Mülhaupt, "Polymers for 3D Printing and Customized Additive Manufacturing," *Chem. Rev.* **117**(15), 10212–10290 (2017).
9. A. Bagheri and J. Jin, "Photopolymerization in 3D Printing," *ACS Appl. Polym. Mater.* **1**(4), 593–611 (2019).
10. J. Zhang and P. Xiao, "3D printing of photopolymers," *Polym. Chem.* **9**(13), 1530–1540 (2018).
11. C. Sun, N. Fang, D. M. Wu, and X. Zhang, "Projection micro-stereolithography using digital micro-mirror dynamic mask," *Sens. Actuators, A* **121**(1), 113–120 (2005).
12. J. R. Tumbleston, D. Shirvanyants, N. Ermoshkin, R. Januszewicz, A. R. Johnson, D. Kelly, K. Chen, R. Pinschmidt, J. P. Rolland, A. Ermoshkin, E. T. Samulski, and J. M. DeSimone, "Continuous liquid interface production of 3D objects," *Science* **347**(6228), 1349–1352 (2015).
13. D. A. Walker, J. L. Hedrick, and C. A. Mirkin, "Rapid, large-volume, thermally controlled 3D printing using a mobile liquid interface," *Science* **366**(6463), 360–364 (2019).
14. S. H. Hsu, T. Chi, J. Kim, P. Somers, B. W. Boudouris, X. Xu, and L. Pan, "High-Speed One-Photon 3D Nanolithography Using Controlled Initiator Depletion and Inhibitor Transport," *Adv. Opt. Mater.* **10**(4), 2102262 (2022).
15. V. Hahn, T. Messer, N. M. Bojanowski, E. R. Curticean, I. Wacker, R. R. Schröder, E. Blasco, and M. Wegener, "Two-step absorption instead of two-photon absorption in 3D nanoprinting," *Nat. Photonics* **15**(12), 932–938 (2021).
16. S. Maruo, O. Nakamura, and S. Kawata, "Three-dimensional microfabrication with two-photon-absorbed photopolymerization," *Opt. Lett.* **22**(2), 132–134 (1997).
17. S. Kawata, H. B. Sun, T. Tanaka, and K. Takada, "Finer features for functional microdevices," *Nature* **412**(6848), 697–698 (2001).
18. P. Mueller, M. Thiel, and M. Wegener, "3D direct laser writing using a 405 nm diode laser," *Opt. Lett.* **39**(24), 6847–6850 (2014).
19. C. Maibohm, O. F. Silvestre, J. Borme, M. Sinou, K. Heggarty, and J. B. Nieder, "Multi-beam two-photon polymerization for fast large area 3D periodic structure fabrication for bioapplications," *Sci. Rep.* **10**(1), 8740 (2020).
20. Z. Wei, T. Sun, S. Shimoda, Z. Chen, X. Chen, H. Wang, Q. Huang, T. Fukuda, and Q. Shi, "Bio-inspired engineering of a perfusion culture platform for guided three-dimensional nerve cell growth and differentiation," *Lab Chip* **22**(5), 1006–1017 (2022).
21. T. Ritacco, D. M. Aceti, G. De Domenico, M. Giocondo, A. Mazzulla, G. Cipparrone, and P. Pagliusi, "Tuning Cholesteric Selective Reflection In Situ Upon Two-Photon Polymerization Enables Structural Multicolor 4D Microfabrication," *Adv. Opt. Mater.* **10**(2), 2101526 (2022).
22. R. M. R. Adão, M. Caño-García, C. Maibohm, and J. B. Nieder, "Photonic polymeric structures and electrostatics simulation method based on a coupled oscillator finite-difference time-domain (O-FDTD) approach," *Opt. Express* **29**(8), 11903–11916 (2021).
23. S. Lightman, M. Bin-Nun, G. Bar, G. Hurvitz, and R. Gvishi, "Structuring light using solgel hybrid 3D-printed optics prepared by two-photon polymerization," *Appl. Opt.* **61**(6), 1434–1439 (2022).
24. T. Aderneuer, O. Fernández, and R. Ferrini, "Two-photon grayscale lithography for free-form micro-optical arrays," *Opt. Express* **29**(24), 39511–39520 (2021).
25. Z. He, Y.-H. Lee, D. Chanda, and S.-T. Wu, "Adaptive liquid crystal microlens array enabled by two-photon polymerization," *Opt. Express* **26**(16), 21184–21193 (2018).
26. C. Wang, Z. Hu, L. Yang, C. Zhang, L. Zhang, S. Ji, L. Xu, J. Li, Y. Hu, D. Wu, J. Chu, and K. Sugioka, "Magnetically driven rotary microfilter fabricated by two-photon polymerization for multimode filtering of particles," *Opt. Lett.* **46**(12), 2968–2971 (2021).
27. B. Xu, W. Q. Du, J. W. Li, Y. L. Hu, L. Yang, C. C. Zhang, G. Q. Li, Z. X. Lao, J. C. Ni, J. R. Chu, D. Wu, S. L. Liu, and K. Sugioka, "High efficiency integration of three-dimensional functional microdevices inside a microfluidic chip by using femtosecond laser multifoci parallel microfabrication," *Sci. Rep.* **6**(1), 1–9 (2016).
28. Z. Lao, N. Xia, S. Wang, T. Xu, X. Wu, and L. Zhang, "Tethered and untethered 3d microactuators fabricated by two-photon polymerization: A review," *Micromachines* **12**(4), 465 (2021).
29. T. Frenzel, V. Hahn, P. Ziemke, J. L. G. Schneider, Y. Chen, P. Kiefer, P. Gumbsch, and M. Wegener, "Large characteristic lengths in 3D chiral elastic metamaterials," *Commun. Mater.* **2**(1), 4–9 (2021).

30. V. Hahn, P. Kiefer, T. Frenzel, J. Qu, E. Blasco, C. Barner-Kowollik, and M. Wegener, "Rapid Assembly of Small Materials Building Blocks (Voxels) into Large Functional 3D Metamaterials," *Adv. Funct. Mater.* **30**(26), 1907795 (2020).
31. S. K. Saha, D. Wang, V. H. Nguyen, Y. Chang, J. S. Oakdale, and S. C. Chen, "Scalable submicrometer additive manufacturing," *Science* **366**(6461), 105–109 (2019).
32. P. Somers, Z. Liang, J. E. Johnson, B. W. Boudouris, L. Pan, and X. Xu, "Rapid, continuous projection multi-photon 3D printing enabled by spatiotemporal focusing of femtosecond pulses," *Light: Sci. Appl.* **10**(1), 199 (2021).
33. D. Yang, L. Liu, Q. Gong, and Y. Li, "Rapid Two-Photon Polymerization of an Arbitrary 3D Microstructure with 3D Focal Field Engineering," *Macromol. Rapid Commun.* **40**(8), 1970017 (2019).
34. J. B. Mueller, J. Fischer, F. Mayer, M. Kadic, and M. Wegener, "Polymerization Kinetics in Three-Dimensional Direct Laser Writing," *Adv. Mater.* **26**(38), 6566–6571 (2014).
35. N. Liaros, S. A. Gutierrez Razo, M. D. Thum, H. M. Ogden, A. N. Zeppuhar, S. Wolf, T. Baldacchini, M. J. Kelley, J. S. Petersen, D. E. Falvey, A. S. Mullin, and J. T. Fourkas, "Elucidating complex triplet-state dynamics in the model system isopropylthioxanthone," *iScience* **25**(1), 103600 (2022).
36. B. Harke, P. Bianchini, F. Brandi, and A. Diaspro, "Photopolymerization inhibition dynamics for sub-diffraction direct laser writing lithography," *ChemPhysChem* **13**(6), 1429–1434 (2012).
37. T. Chi, P. Somers, D. A. Wilcox, A. J. Schuman, J. E. Johnson, Z. Liang, L. Pan, X. Xu, and B. W. Boudouris, "Substituted Thioxanthone-Based Photoinitiators for Efficient Two-Photon Direct Laser Writing Polymerization with Two-Color Resolution," *ACS Appl. Polym. Mater.* **3**(3), 1426–1435 (2021).
38. L. Yang, A. Münchinger, M. Kadic, V. Hahn, F. Mayer, E. Blasco, C. Barner-Kowollik, and M. Wegener, "On the Schwarzschild Effect in 3D Two-Photon Laser Lithography," *Adv. Opt. Mater.* **7**(22), 1901040 (2019).
39. R. Pingali and S. K. Saha, "Reaction-Diffusion Modeling of Photopolymerization During Femtosecond Projection Two-Photon Lithography," *J. Manuf. Sci. Eng.* **144**(2), 021011 (2022).
40. M. G. Guney and G. K. Fedder, "Estimation of line dimensions in 3D direct laser writing lithography," *J. Micromechanics Microengineering* **26**(10), 105011 (2016).
41. N. Uppal and P. S. Shiakolas, "Modeling of temperature-dependent diffusion and polymerization kinetics and their effects on two-photon polymerization dynamics," *J. Micro/Nanolith. MEMS MOEMS* **7**(4), 043002 (2008).
42. A. Pikulin and N. Bityurin, "Spatial resolution in polymerization of sample features at nanoscale," *Phys. Rev. B: Condens. Matter Mater. Phys.* **75**(19), 195430 (2007).
43. T. Chi, P. Somers, D. A. Wilcox, A. J. Schuman, V. Iyer, R. Le, J. Gengler, M. Ferdinandus, C. Liebig, L. Pan, X. Xu, and B. W. Boudouris, "Tailored thioxanthone-based photoinitiators for two-photon-controllable polymerization and nanolithographic printing," *J. Polym. Sci., Part B: Polym. Phys.* **57**(21), 1462–1475 (2019).
44. J. Fischer, G. Von Freymann, and M. Wegener, "The materials challenge in diffraction-unlimited direct-laser-writing optical lithography," *Adv. Mater.* **22**(32), 3578–3582 (2010).
45. B. Chakraborty, K. S. Gupta, S. Sen, G. P. Srivastava, I. O. Thomas, Y. Li, F. Qi, H. Yang, Q. Gong, X. Dong, and X. Duan, "Nonuniform shrinkage and stretching of polymerized nanostructures fabricated by two-photon photopolymerization," *Nanotechnology* **19**(5), 055303 (2008).
46. H. B. Sun, T. Suwa, K. Takada, R. P. Zaccaria, M. S. Kim, K. S. Lee, and S. Kawata, "Shape precompensation in two-photon laser nanowriting of photonic lattices," *Appl. Phys. Lett.* **85**(17), 3708–3710 (2004).
47. J. Purtov, A. Verch, P. Rogin, and R. Hensel, "Improved development procedure to enhance the stability of microstructures created by two-photon polymerization," *Microelectron. Eng.* **194**, 45–50 (2018).
48. N. Yoshimura, S. Maruo, and T. Hasegawa, "Single-anchor support and supercritical CO₂ drying enable high-precision microfabrication of three-dimensional structures," *Opt. Express* **17**(23), 20945–20951 (2009).
49. B. Harke, W. Dallari, G. Grancini, D. Fazzi, F. Brandi, A. Petrozza, and A. Diaspro, "Polymerization inhibition by triplet state absorption for nanoscale lithography," *Adv. Mater.* **25**(6), 904–909 (2013).
50. X. Allonas, C. Ley, C. Bibaut, P. Jacques, and J. P. Fouassier, "Investigation of the triplet quantum yield of thioxanthone by time-resolved thermal lens spectroscopy: Solvent and population lens effects," *Chem. Phys. Lett.* **322**(6), 483–490 (2000).
51. J. Christmann, X. Allonas, C. Ley, A. Ibrahim, and C. Croutxé-Barghorn, "Triazine-Based Type-II Photoinitiating System for Free Radical Photopolymerization: Mechanism, Efficiency, and Modeling," *Macromol. Chem. Phys.* **218**(18), 1600597 (2017).
52. R. Mundt, T. Villnow, C. T. Ziegenbein, P. Gilch, C. Marian, and V. Rai-Constapel, "Thioxanthone in apolar solvents: Ultrafast internal conversion precedes fast intersystem crossing," *Phys. Chem. Chem. Phys.* **18**(9), 6637–6647 (2016).
53. F. Burmeister, S. Steenhusen, R. Houbertz, U. D. Zeitner, S. Nolte, and A. Tünnermann, "Materials and technologies for fabrication of three-dimensional microstructures with sub-100 nm feature sizes by two-photon polymerization," *J. Laser Appl.* **24**(4), 042014 (2012).
54. H. Duran, S. Meng, N. Kim, J. Hu, T. Kyu, L. V. Natarajan, V. P. Tondiglia, and T. J. Bunning, "Kinetics of photopolymerization-induced phase separation and morphology development in mixtures of a nematic liquid crystal and multifunctional acrylate," *Polymer* **49**(2), 534–545 (2008).
55. C. Decker and A. D. Jenkins, "Kinetic Approach of Oxygen Inhibition in Ultraviolet and Laser-Induced Polymerizations," *Macromolecules* **18**(6), 1241–1244 (1985).
56. M. H. Schneider, Y. Tran, and P. Tabeling, "Benzophenone absorption and diffusion in poly(dimethylsiloxane) and its role in graft photo-polymerization for surface modification," *Langmuir* **27**(3), 1232–1240 (2011).

57. S. Yoshida, Y. Takahata, S. Horiuchi, H. Kurata, and M. Yamamoto, "Numerical model of radical photopolymerization based on interdiffusion," *Int. J. Polym. Sci.* **2014**, 243895 (2014).
58. M. Wen and A. V. McCormick, "Kinetic model for radical trapping in photopolymerization of multifunctional monomers," *Macromolecules* **33**(25), 9247–9254 (2000).
59. L. L. Fillbrook, M. D. Nothling, M. H. Stenzel, W. S. Price, and J. E. Beves, "Rapid Online Analysis of Photopolymerization Kinetics and Molecular Weight Using Diffusion NMR," *ACS Macro Lett.* **11**(2), 166–172 (2022).
60. J. B. Mueller, J. Fischer, Y. J. Mange, T. Nann, and M. Wegener, "In-situ local temperature measurement during three-dimensional direct laser writing," *Appl. Phys. Lett.* **103**(12), 123107 (2013).
61. J. Fischer, J. B. Mueller, J. Kaschke, T. J. A. Wolf, A.-N. Unterreiner, and M. Wegener, "Three-dimensional multi-photon direct laser writing with variable repetition rate," *Opt. Express* **21**(22), 26244–25260 (2013).
62. W. Haske, V. W. Chen, J. M. Hales, W. Dong, S. Barlow, S. R. Marder, and J. W. Perry, "65 nm feature sizes using visible wavelength 3-D multiphoton lithography," *Opt. Express* **15**(6), 3426–3436 (2007).
63. Z. Tomova, N. Liaros, S. A. Gutierrez Razo, S. M. Wolf, and J. T. Fourkas, "In situ measurement of the effective nonlinear absorption order in multiphoton photoresists," *Laser Photonics Rev.* **10**(5), 849–854 (2016).
64. N. Liaros and J. T. Fourkas, "Methods for Determining the Effective Order of Absorption in Radical Multiphoton Photoresists: A Critical Analysis," *Laser Photonics Rev.* **15**(1), 2000203 (2021).
65. X. Zhou, Y. Hou, and J. Lin, "A review on the processing accuracy of two-photon polymerization," *AIP Adv.* **5**(3), 030701 (2015).
66. J. Serbin, A. Egbert, A. Ostendorf, B. N. Chichkov, R. Houbertz, G. Domann, J. Schulz, C. Cronauer, L. Fröhlich, and M. Popall, "Femtosecond laser-induced two-photon polymerization of inorganic–organic hybrid materials for applications in photonics," *Opt. Lett.* **28**(5), 301–303 (2003).
67. B. Cardenas-Benitez, C. Eschenbaum, D. Mager, J. G. Korvink, M. J. Madou, U. Lemmer, I. De Leon, and S. O. Martinez-Chapa, "Pyrolysis-induced shrinking of three-dimensional structures fabricated by two-photon polymerization: experiment and theoretical model," *Microsyst. Nanoeng.* **5**(1), 38 (2019).
68. S. R. Cohen and J. T. Fourkas, "Extracting Information on Linear and Nonlinear Absorption from Two-Beam Action Spectroscopy Data," *J. Phys. Chem. A* **123**(33), 7314–7322 (2019).
69. J. Fischer and M. Wegener, "Three-dimensional direct laser writing inspired by stimulated-emission-depletion microscopy [Invited]," *Opt. Mater. Express* **1**(4), 614–624 (2011).